Volume 1 | Number 1 | Jan 2013 | Pages 1–100

PCCP

Physical Chemistry Chemical Physics
www.rsc.org/pccp

ROYAL SOCIETY OF CHEMISTRY

ROYAL SOCIETY OF CHEMISTRY

www.rsc.org/pccp

ARTICLE

NiCo2S4 nanotube arrays grown on flexible nitrogen-doped carbon foams as three-dimensional binder-free integrated anodes for high-performance lithium-ion batteries

Xiaoyu Wu, Songmei Li,[*] Bo Wang, Jianhua Liu, and Mei Yu

Binary metal sulfides, especially NiCo2S4, hold great promise as anode materials for high-performance lithium-ion batteries because of their excellent electronic conductivity and high capacity compared to mono-metal sulfides and oxides. Here, NiCo2S4 nanotube arrays are successfully grown on flexible nitrogen-doped carbon foam (NDCF) substrates with robust adhesion via a facile surfactant-assisted hydrothermal route and the subsequent sulfurization treatment. The obtained NiCo2S4/NDCF composites show unique three-dimensional architectures, in which NiCo2S4 nanotubes with a length of ~5 μm and 100 nm in width are uniformly grown on the NDCF skeletons to form arrays. When served directly as integrated anodes for lithium-ion batteries without any conductive additives and binders, the NiCo2S4/NDCF composites exhibit a high reversible capacity of 1721 mAh g^{-1} at a high current density of 500 mA g^{-1}, enhanced cycling performance with the capacity maintaining at 1182 mAh g^{-1} after 100 cycles, and a remarkable rate capability. The excellent lithium storage performances of the composites could be attributed to the unique material composition, rationally designed hollow nanostructure and integrated smart architecture, which offers fast electron transport and ion diffusion, enhanced material-electrolyte contact area and facile accommodation of the strains during the lithium insertion and extraction process.

1. Introduction

Rechargeable lithium-ion batteries (LIBs) have gained commercial success as the leading power source for portable electronics, and have shown great promise in upcoming large-scale applications because of their inherent advantages including high energy density, long life span, lack of memory effect and environmental nontoxicity.[1-4] The ever-growing market demands for LIBs have stimulated numerous research efforts aiming at the exploration of novel electrode materials with higher capacity and long-term cycling stability.[5-8] Meanwhile, in order to further facilitate the portability of next-generation LIBs, designing and developing alternative electrode materials with flexibility, light-weight, bendability and safety

has been considered as one of the most effective approaches.[9,10]

Among the great variety of anode materials studied, electrochemical active metal oxides (MOs) and sulfides (MSs), such as Co3O4, SnO2, MoO, MoS2, ZnS and CoS2, have attracted extensive attention because of their high theoretical capacities, low cost, and environmental friendliness.[11-17] Importantly, MSs generally feature higher electrical conductivity, better mechanical and thermal stability, and higher redox reversibility than their MOs counterparts.[18,19] In particular, binary metal sulfide NiCo2S4 exhibits an excellent electrical conductivity, at least two orders of magnitude higher than that of NiCo2O4 and ~10^4 times higher than conventional MOs, and possesses higher electrochemical activity and capacity than the corresponding mono-metal sulfides, indicating its great potential as high-performance anode material for LIBs.[18,20-22] In previous studies, various NiCo2S4 nanostructures including nanosheets, nanowires, nanotubes and nanonetworks have been synthesized and exhibit remarkable electrochemical performance with high capacitance and long cycle life when used as electrode for supercapacitors.[18,22-25] However, there are few studies on NiCo2S4-based materials

Key Laboratory of Aerospace Advanced Materials and Performance of Ministry of Education, School of Materials Science and Engineering, Beihang University, Beijing, 100191, China.
E-mail: songmei_li@buaa.edu.cn; Fax: +86-10-82317103; Tel: +86-10-82317103

used as anodes for LIBs. Based on the considerations above, it is an urgent requirement to further develop $NiCo_2S_4$-based anode materials for high-performance LIBs. However, it is noteworthy that MSs, $NiCo_2S_4$ included, still suffer from large volumetric changes during charge/discharge process, resulting in low capacity and poor cycling stability.[18,26] Therefore, designing $NiCo_2S_4$-based anode materials with novel architectures of high effective surface area to buffer the volumetric changes and short the diffusion distances of electron and ion are of great significance.

Recently, fabricating integrated binder-free electrodes by directly coating active materials on self-supported three-dimensional (3D) porous conducting substrate has emerged as a new direction. The integrated electrodes can avoid the use of any binder or conductive additives, offer a larger electrode/electrolyte contact area, and provide 3D interconnected network pathways for both electron and ion, resulting in efficient reaction kinetics during the charge/discharge process.[22,27] Among the various 3D conducting substrates, carbonaceous interpenetrating structures are considered to be the most attractive current collectors to support electroactive materials because of their high surface area, good flexibility and light weight.[10,22,27-30] However, it is difficult to large-scale produce 3D carbonaceous structures such as carbon nanotubes sponge and graphene foams because of their complex preparation processes and relatively high-cost.[31,32] And considering the potential incompatibility issue between electroactive materials and conductive skeleton, the direct growth of electroactive materials with optimal nanostructures on 3D conductive substrates still remains a lot of challenges.[22] Therefore, developing a novel and easily-prepared 3D carbonaceous structures, and improving the growth strategy to achieve a robust 3D carbonaceous structure-backboned $NiCo_2S_4$ architecture with superior lithium storage properties are urgent in the field of LIBs.

Here, we focus on the development of a nitrogen-doped carbon foam (NDCF) based 3D electrodes architectures for LIBs, which can achieve a simultaneous improvement in the form factor flexibility, light weight, specific capacity and cycling performance. The NDCF with 3D interconnected network is prepared by the direct carbonization of commercially available melamine foam, which exhibits enhanced electronic conductivity and improved surface performance of the microfibers to facilitate the uniform fabrication of active materials on it compared to traditional 3D carbonaceous substrates.[24,33,34] Uniform $NiCo_2S_4$ nanotubes arrays are successfully grown on NDCF with robust adhesion via a surfactant-assisted hydrothermal process followed by a facile sulfurization treatment. When directly served as anodes for LIBs without any carbon additives or binders, the resultant $NiCo_2S_4$/NDCF composites exhibit high specific capacity, excellent rate capability and improved cycling stability even at high current densities compared to the binder-containing counterparts, which could be attributed to their unique hollow nanotube structures and integrated smart 3D architectures.

Experimental

Materials and Methods

Synthesis of NDCF: The commercially available melamine foams were carbonized at a rate of 5 ℃ min^{-1} in nitrogen atmosphere up to 800 ℃ and held at the final temperature for 2 h, and then naturally cooled down to room temperature.

Growth of $NiCo_2S_4$ nanotube arrays on NDCF: In a typical process, 2 mmol $Co(NO_3)_2$ $6H_2O$, 1 mmol of $NiCl_2$ $6H_2O$, 3.6 mmol urea and 0.8 mmol hexadecyl trimethyl ammonium bromide (CTAB) were dissolved into 20 mL of deionized water to form a transparent pink solution with continuous stirring. After putting a piece of NDCF (ca. 40 mm × 20 mm × 0.5 mm), the solution was then transferred to a 25 mL Teflon-lined stainless steel autoclave and kept at 120 ℃ for 3 h, and then cooled down to room temperature. After hydrothermal growth, the NDCF covered with NiCo-precursors was taken out and carefully rinsed several times with deionized water and absolute ethanol. Then, the NiCo-precursor/NDCF composites were immersed in 0.1 M Na_2S solution and kept at 160 ℃ for 6 h. After cooling down naturally to the room temperature, the as-prepared $NiCo_2S_4$/NDCF composites were taken out and washed with deionized water and absolute ethanol for several times, then dried at 60 ℃ for 12 h. For comparison, $NiCo_2S_4$ powders were also prepared in a similar manner without use of NDCF substrates.

Microscopic Characterization

The crystallographic structure of the as-prepared products were determined by a powder X-ray diffraction system (XRD, Rigaku D/max 2200PC) equipped with Cu Kα radiation (λ=0.15418 nm) with the diffraction angle in the range of 10-70 °. The morphologies and microstructures of the products were characterized by field-emission scanning electron microscope (FE-SEM, JEOL JSM-7500F) and transmission electron microscope (TEM, JEOL JEM-2100F). And the chemical compositions of the products were analyzed by X-ray photoelectron spectroscope (XPS, AXIS UTLTRADLD equipped with a dual Mg Ka-Al Ka anode for photoexcitation). The N_2 adsorption-desorption were determined by Brunauer-Emmett-Teller (BET) measurements using an ASAP-2010 surface area analyzer.

Electrochemical Performance Measurements

The electrochemical performance of the as-prepared products was performed at room temperature using CR2025 coin-type cells assembled in an argon-filled glove box, in which the contents of oxygen and water were less than 1 ppm. For the coin-cell assembly, the pure NDCF and $NiCo_2S_4$/NDCF composites were punched in the form of 12 mm diameter disks with a thickness of o.5 mm, and then used directly as the working electrode without any conductive additives and polymer binders. Calculated by weighting the total mass of 30 pieces of pure NDCF and $NiCo_2S_4$/NDCF composites, respectively, the average weight of the active material ($NiCo_2S_4$)

for each $NiCo_2S_4$/NDCF electrode was about 1.4 mg, thus the corresponding specific mass loading of the active material was about 1.2 mg cm^{-2}. A metallic lithium foil served as both the counter electrode and the reference electrode, a polypropylene (PP) microporous film (Celgard 2400) was used as the separator, and a solution of 1 M $LiPF_6$ dissolved in a 1:1 (v/v) mixture of ethylene carbonate (EC) and dimethyl carbonate (DMC) was used as electrolyte. For comparison, the $NiCo_2S_4$ powders were also formed into working electrodes. The $NiCo_2S_4$ powders were mixed with the conductive carbon black and polyvinylidene fluoride (PVDF) binder in a weight ratio of approximately 8:1:1, forming N-methylpyrrolidinone (NMP) slurry. And then the slurry was directly coated on copper foil current collectors and dried overnight in a vacuum oven at 60 ºC to fabricate the pasted electrode of $NiCo_2S_4$ powders.

The cyclic voltammetry (CV) and galvanostatic charge-discharge measurements were conducted using LAND CT2001A battery-testing instrument and multichannel Arbin BT2000 system in the voltage range of 0.005-3.0 V (vs. Li$^+$/Li). Electrochemical impedance spectroscopy (EIS) measurements were performed using an electrochemistry system (PARSTAT 2273, Princeton Applied Research, USA) by applying a AC voltage amplitude of 5 mV in the frequency range from 100 kHz to 0.01 Hz.

Results and discussion

The NDCF, which is obtained from the carbonization of commercially available melamine foam at 800 ℃ for 2 h in an inert atmosphere, is considered as an ideal substrate to construct anodes for LIBs. As shown in Fig. 1(a), the NDCF can sustain a large-strain compressing or bending deformation, and recovers most of its volume elastically, indicating its good resilience and flexibility. According to the SEM images shown in Fig. 1(b), the NDCF exhibit unique 3D interconnected network architecture composed of branched fibers with a diameter of several micrometers. Importantly, the XPS spectra in Fig. 1(c) confirm the nitrogen incorporation in the carbon microfibers, which is efficient to enhance the electronic conductivity of
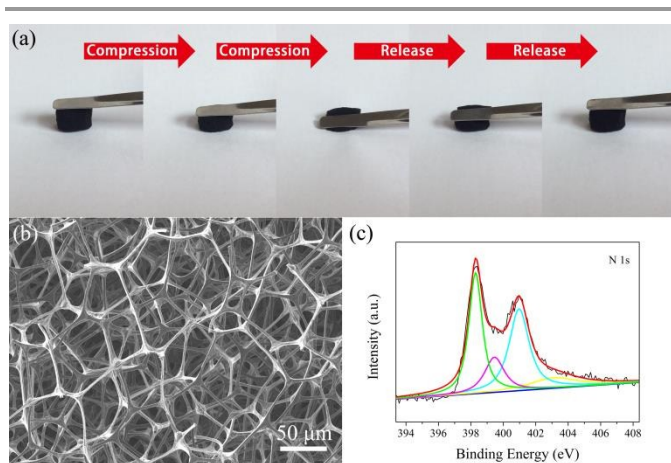
Fig. 1 (a) Mechanical properties of NDCF; (b) SEM images of NDCF; (c) High-resolution XPS spectra of N 1s for NDCF.
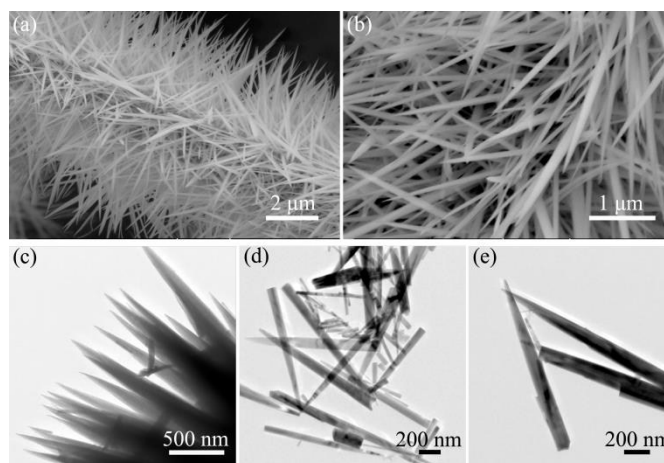
Fig. 2 (a,b) Typical SEM images of NiCo-precursors grown on NDCF at different magnifications; (c-e) TEM images of NiCo-precursors scratched from NDCF at different magnifications.

carbon materials because of its electron-donor properties.[33,34] Moreover, nitrogen doping also helps to improve the surface performance of the microfibers to facilitate the uniform loading of active materials on it. [35] In addition, the NDCF is extremely lightweight with a density of ~ 5 mg cm^{-3}. Benefiting from the advantages mentioned above, the NDCF substrates are expected to play a significant role in improving the lithium storage properties of the $NiCo_2S_4$/NDCF composites.

The $NiCo_2S_4$/NDCF composites are synthesized via a facile two-step method, involving the hydrothermal growth of NiCo-precursors on NDCF substrates and subsequent conversion into $NiCo_2S_4$ through sulfurization treatment. The morphology and microstructure of the products were investigated by FE-SEM and TEM. As shown in the SEM images of the products obtained after the hydrothermal reaction (Fig. 2(a, b)), uniform nanowire arrays of the NiCo-precursors are successfully grown on the skeletons of the NDCF substrates. After sulfurization process, the NiCo-precursors are converted into $NiCo_2S_4$. As seen from the SEM images of the $NiCo_2S_4$/NDCF composites in Fig. 3, a large scale of $NiCo_2S_4$ architectures with a length of ~5 μm are uniformly grown on the NDCF skeletons to form nanowire-like arrays, preserving the general morphology of the NiCo-precursors. Interestingly, the $NiCo_2S_4$ architectures exhibit unique hollow nanotube structures, as shown in the TEM images of the $NiCo_2S_4$ products scratched from the $NiCo_2S_4$/NDCF composites (Fig. 4(a)), which is quite different from the solid structures of the NiCo-precursor nanowires (Fig. 2(c-e)). In comparison, the $NiCo_2S_4$ powders prepared without the use of NDCF substrates exhibit the morphology of aggregated nanotubes, as shown in Fig. S1 (Supporting Information). According to previous literatures, the formation of the hollow nanotube structure can be attributed to Kirkendall effect during the sulfurization process.[35-37] Fig. 4(b, c) provide further insight into the detailed structures of the $NiCo_2S_4$ nanotubes, in which the inner hollow nanostructure is clear distinguished. As shown in Fig. 4(b, c),

This journal is © The Royal Society of Chemistry 2015

Phys. Chem. Chem. Phys., 2015, **00**, 1-3 **00**, 1-3 | **3**
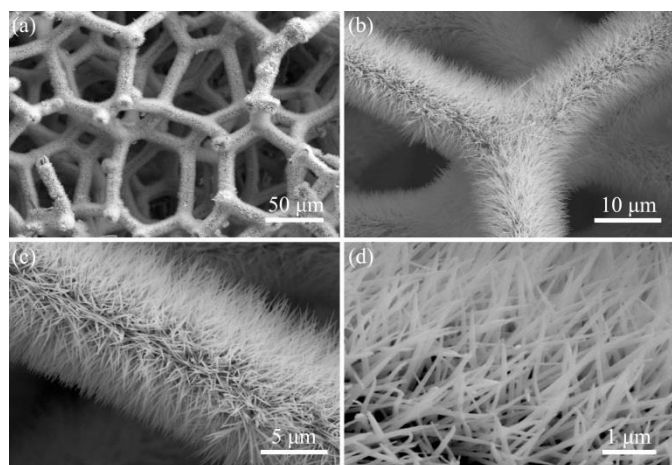
Fig. 3 Typical SEM images of the $NiCo_2S_4$/NDCF composites at different magnifications.

the $NiCo_2S_4$ nanotube exhibits a shell thickness of ~16 nm, and its width is about 100 nm. In addition, it is found that numerous pores are distributed on wall of the nanotubes, which are resulted from the continuous outward ion diffusion during the reaction, and can provide sufficient free space to further ameliorate the tendency for expansion.[34] In this sense, such a well-designed composite judiciously combines the advantages of the $NiCo_2S_4$ nanotube arrays (high capacity, large specific surface area as well as effective relief of volumetric change) and 3D-structured NDCF substrate (high electronic conductivity, good flexibility, light-weight, and fast mass and electron transport kinetics), thus holding great promise to be a high-performance anode material with excellent cycling stability and good rate performance.[38] Moreover, the lattice spacing of 0.33 nm corresponds to the (220) crystal plane of cubic phase $NiCo_2S_4$, as shown in the high-resolution transmission electron microscopy (HRTEM) image in Fig. 4(d). And the selected area electron diffraction (SAED) pattern (Fig. 4(e)) reveals the polycrystalline nature of the nanotubes, in
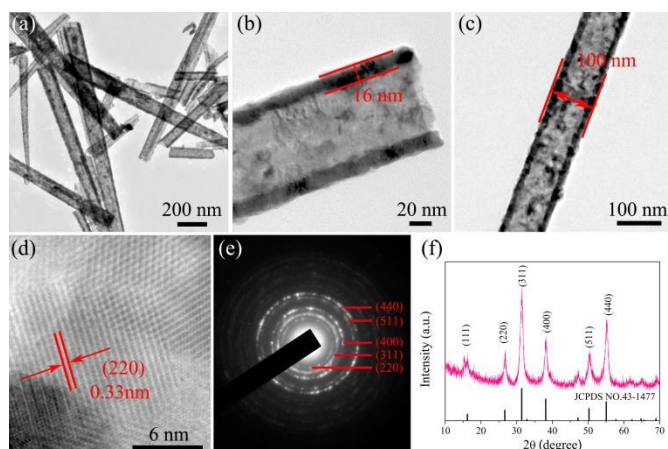
which the diffraction rings can be readily indexed to the (220), (311), (400), (511) and (440) planes of the $NiCo_2S_4$ crystal structure (JCPDF No.43-1477).

The phase structures of the as-prepared products were further analyzed by X-ray diffraction. Fig. S2 (Supporting Information) displays a typical XRD pattern of the NiCo-precursor, in which all the reflection peaks could be well indexed to crystalline $Ni_{2/3}Co_{4/3}(CO_3)(OH)_2$.[23,39] Importantly, the XRD pattern of the precursor exhibits almost the same pattern as that of $Co(CO_3)_{0.5}(OH)$ $0.11H_2O$ (JCPDS No.48-0083), indicating the stability of the crystal structure with the partial substitution of Co ions by Ni ions.[23] The XRD pattern of the $NiCo_2S_4$ nanotubes scratched from NDCF substrates and the standard XRD pattern of cubic $NiCo_2S_4$ are presented in Fig. 4(f). The diffraction peaks at 15.4°, 26.8°, 31.6°, 38.3°, 47.4°, 50.5° and 55.3° can be well indexed to the (111), (220), (311), (400), (511) and (440) planes of the cubic $NiCo_2S_4$ phase, respectively, in agreement with the standard XRD pattern of cubic $NiCo_2S_4$ (JCPDS No. 43-1477).[23,39,40] No other diffraction peaks were observed, verifying that the Ni-Co precursors have been fully converted to phase-pure $NiCo_2S_4$ after sulfurization process. The specific surface area and pore size distribution of the $NiCo_2S_4$/NDCF composites were determined by the full nitrogen adsorption and desorption isotherms. As shown in Fig. S3 (Supporting Information), a type-IV isotherm with a distinct type-H3 hysteresis loop in the relative pressure range of 0.45–1.0 P/P_0 can be observed, which is ascribed to the presence of a mesoporous structure in the composites, consistent with the TEM results mentioned above.[41,42] As determined by N_2 sorption measurements (Fig. S3, Supporting Information), the $NiCo_2S_4$/NDCF composites possess a Brunauer-Emmett-Teller (BET) specific surface area of 41.84 $m^2 g^{-1}$.

X-ray photoelectron spectroscopy (XPS) measurements were conducted to evaluate the elemental composition and chemical state of the as-prepared $NiCo_2S_4$, and the results are presented in Fig.5. The survey spectrum (Fig. 5(a)) indicates

Fig. 4 (a–c) TEM images, (d) HRTEM images, (e) corresponding SAED pattern and (f) XRD pattern of the $NiCo_2S_4$ nanotubes scratched from NDCF.
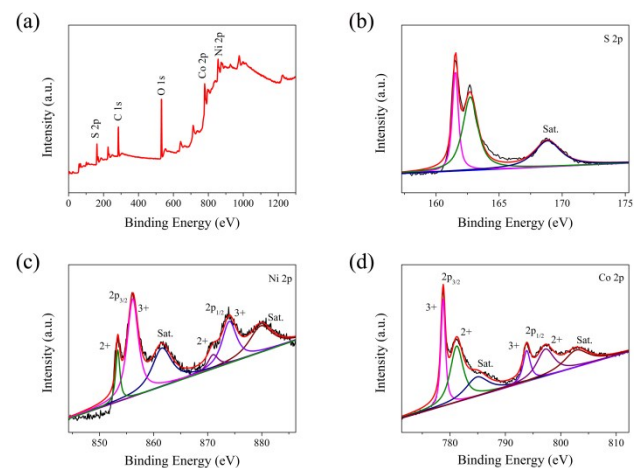
Fig. 5 (a) XPS survey spectra and high-resolution XPS spectra of (b) S 2p, (c) Ni 2p, and (d) Co 2p for the $NiCo_2S_4$ nanotubes scratched from NDCF.

the presence of Ni, Co, and S, while the C element is from a reference for normalization and O element is due to exposure to the air. By using a Gaussian fitting method, the Ni 2p spectrum (Fig. 5(c)) can be well fitted with two spin-orbit doublets and two shake-up satellites (indicated as "Sat."). The deconvolution of the Ni 2p peaks show the atoms in $2p_{3/2}$ electronic configuration at 853.4 and 856.2 eV, indicating that it is in the divalent and trivalent states, and the peaks at ~872 eV corresponds to the Ni $2p_{1/2}$ band.[38] The Co 2p spectrum (Fig. 5(d)) can also be best fitted with two spin-orbit doublets characteristic of Co^{2+} and Co^{3+}, and two shake-up satellites. Fig. 5(b) shows the core-level spectrum of the S 2p region, which can be divided into two main peaks at around 163.5 and 162.1 eV and one shake-up satellite at about 169.0 eV. The component at 162.1 eV is characteristic of S^{2-}, while the component at 163.5 eV can be attributed to the sulphur ion in low coordination at the surface.[21,25,38,43] These results indicate that the chemical composition of $NiCo_2S_4$ contain Co^{2+}, Co^{3+}, Ni^{2+}, Ni^{3+} and S^{2-}, which are in good agreement with the results in previous literatures for $NiCo_2S_4$.[21,25,40,43,44]

Based on the above results, the possible formation mechanism of the $NiCo_2S_4$/NDCF composites has been concluded and illustrated in Fig. 6. It clearly shows that the whole process involves two steps: (1) surfactant-assisted hydrothermal growth of NiCo-precursor nanowires on NDCF; (2) sulfurization process of the NiCo-precursor nanowires into $NiCo_2S_4$ nanotubes on the basis of the Kirkendall effect.[35,37] During the first hydrothermal growth process, the $Ni_{2/3}Co_{4/3}(CO_3)(OH)_2$ (denoted as NiCo-precursor) nanowire arrays are in situ grow on the NDCF substrates by hydrothermal treating Ni^{2+} and Co^{2+} in the presence of urea and CTAB. As for the next step, the as-fabricated NiCo-precursor nanowire arrays supported on NDCF are converted to the $NiCo_2S_4$ nanotube arrays counterpart by reacting with sodium sulphide (Na_2S). In this process, the well-known anion-exchange reaction based on Kirkendall effect, which has been used to guide the growth of various hollow nanoparticles and nanotubes, can best explain the conversion of the $Ni_{2/3}Co_{4/3}(CO_3)(OH)_2$ nanowires into $NiCo_2S_4$ nanotubes on NDCF.[45,46] It is noteworthy that the anion-exchange reaction are accompanied with partial change of the oxidation state of Co and Ni cations, which is consistent with the previous literatures.[21,47,48] Firstly, S^{2-} anions in the solution exchange with CO_3^{2-} and OH^- anions of $Ni_{2/3}Co_{4/3}(CO_3)(OH)_2$ to form a thin layer of $NiCo_2S_4$ nanoparticles at the surface of the nanowires, which acts as a physical barrier to prevent the direct chemical reaction between outside S^{2-} ions and inner $Ni_{2/3}Co_{4/3}(CO_3)(OH)_2$.[21,38] And the CO_3^{2-} and OH^- anions can react with H^+ cations in the solution to produce CO_2 and H_2O.[21] Under these circumstances, further reaction depends on the spontaneously outward diffusion of the inner ions from $Ni_{2/3}Co_{4/3}(CO_3)(OH)_2$ to the external surface of the nanowires through this newly formed $NiCo_2S_4$ shell, which provides a source of $Ni_{2/3}Co_{4/3}(CO_3)(OH)_2$ for further anion exchange and the growth of the $NiCo_2S_4$.[21,38] Because the outward diffusion rate of the cobalt and nickel source is faster than the inward transport rate of S^{2-} ions, this unequal diffusion
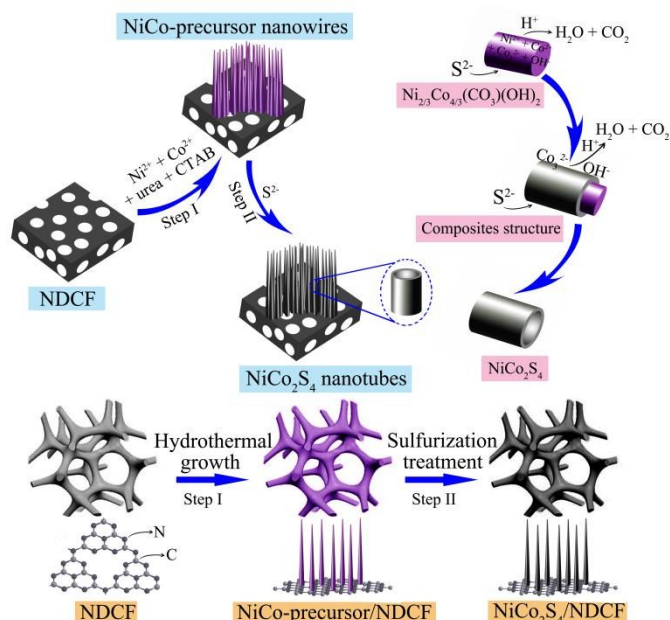
Fig. 6 Schematic illustrations of the formation process of the $NiCo_2S_4$/NDCF composites

of reacting species would produce voids at the center of the obtained nanotube.[38] With the reaction processing, the $NiCo_2S_4$ shell will be increased and the $Ni_{2/3}Co_{4/3}(CO_3)(OH)_2$ core is gradually decreased, thus finally forming hollow $NiCo_2S_4$ nanotubes.

The obtained $NiCo_2S_4$/NDCF composites were directly used as anodes for LIBs without binder or conductive additives, and exhibit remarkable electrochemical performances as shown in Fig. 7. As mentioned above, the electrochemical performances of traditional slurry-coating electrodes of $NiCo_2S_4$ powders were evaluated as a control experiment for comparison, and the lithium storage performance of the pure NDCF electrodes was also evaluated. Cyclic voltammetry (CV) measurements were conducted to identify the electrochemical reactions occurred during the lithiation/delithiation process of the electrodes. Fig. 7(a) displays the initial four consecutive CV curves of the $NiCo_2S_4$/NDCF electrode at a scan rate of 0.1 mV s^{-1} between 0.005 and 3.0 V (vs. Li$^+$/Li). In the first cathodic scan, two intense peaks located at ~1.10 V and 1.40 V are observed, which can be attributed to the Li$^+$ insertion into $NiCo_2S_4$ to form $Li_xNiCo_2S_4$.[49] And several weak peaks located at ~0.73 V can be assigned to subsequent conversion of Li with $NiCo_2S_4$, as well as the decomposition of organic electrolyte to form a solid electrolyte interphase (SEI) layer at the electrode-electrolyte interface.[49,50] The large peak in the potential range from 0.005 to 0.39 corresponds with the insertion of Li$^+$ into NDCF, which is electroactive for lithium storage as confirmed in the CV curves of pure NDCF electrode in Fig.S4 (Supporting information).[47] During the first anodic scan, the broad peaks at ~ 2.25 V and 1.54 V could be ascribed to reverse extraction of Li$^+$, resulting in the formation of NiS$_x$ and CoS$_x$.[18] In the second and following cycles, the main cathodic peaks shift toward a

This journal is © The Royal Society of Chemistry 2015

Phys. Chem. Chem. Phys., 2015, **00**, 1-3 **00**, 1-3 | **5**
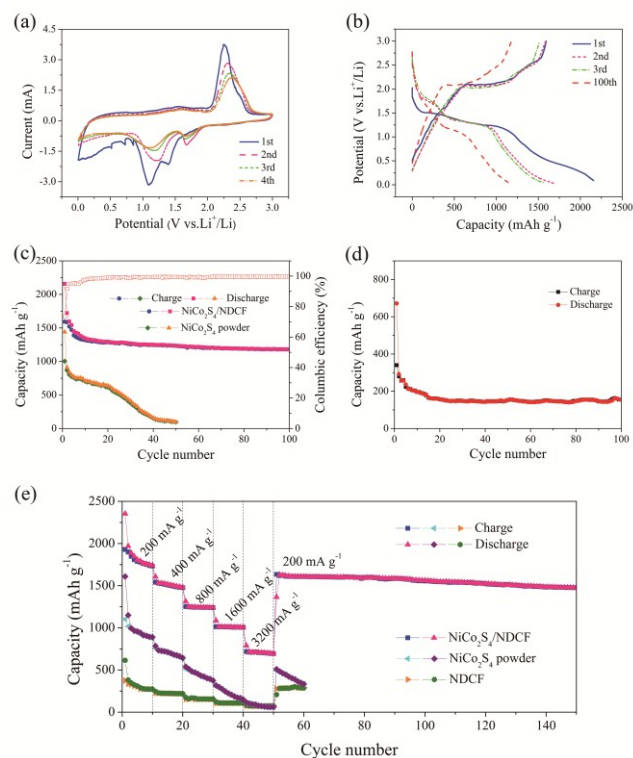
Fig. 7 (a) Cyclic voltammograms of the NiCo$_2$S$_4$/NDCF electrode for the initial four cycles at a scan rate of 0.1 mV s^{-1} in the voltage range of 0.005-3.0 V; (b) Charge-discharge voltage profiles of the NiCo$_2$S$_4$/NDCF electrode at a current density of 500 mA g^{-1}; (c) Comparison of cycling performance of the NiCo$_2$S$_4$/NDCF electrode and NiCo$_2$S$_4$ powders pasted electrode at a current density of 500 mA g^{-1}, and the corresponding Coulombic efficiency of the NiCo$_2$S$_4$/NDCF electrodes; (d) Cycling performance of the pure NDCF electrode at a current density of 200 mA g^{-1}; (e) Comparison of rate capability of the NiCo$_2$S$_4$/NDCF electrode, NiCo$_2$S$_4$ powders pasted electrode and pure NDCF electrode.

higher potential, which is related to the occurrence of certain irreversible reactions accompanying with the formation of a SEI layer on the electrode surface.[18,51,52] Obviously, the CV curves of the second and following cycles are different from that of the first cycle, which correspond to the reactions between Li$^+$ and NiS$_x$, CoS$_x$ as well as NDCF, instead. Meanwhile, the slight differences of the oxidation and reduction peaks between the two cycles and the subsequent cycles are possibly due to the gradual building of the SEI layers through a formation, partial decomposition and reformulation procedure, which has been observed in previous literatures.[50,53,54] And in the subsequent cycles, the peaks are almost overlapped, presenting the gradually established good reversible performances.[18]

To gain further information on the electrochemical performance of the electrodes, galvanostatic charge-discharge tests were conducted at a current density of 500 mA g^{-1} in the voltage window of 0.005-3.0 V (vs. Li$^+$/Li). Fig. 7(b) shows the

charge-discharge profiles of the NiCo$_2$S$_4$/NDCF electrode in the 1st, 2nd, 3rd and 100th cycles. As seen in Fig. 7(b), the first cycle reveals discharge and charge capacities of 2157 mAh g^{-1} and 1593 mAh g^{-1}, respectively, indicating an initial Coulombic efficiency of 73.8%. The irreversible capacity loss for the first cycle can be attributed to the possible incomplete restoration of metallic Ni and Co into the original sulfide and the formation of the SEI layers, which has been commonly observed in NiCo$_2$S$_4$ electrode materials.[18,55,56] In the second cycle, the discharge and charge capacities of the NiCo$_2$S$_4$/NDCF electrode are 1721 and 1586 mAh g^{-1}, respectively, and the Coulombic efficiency rapidly rises to 92.1%. Fig. 7(c) compares the cycling performance of the NiCo$_2$S$_4$/NDCF electrode and NiCo$_2$S$_4$ powders pasted electrode. As shown in Fig. 7(c), the discharge capacities of the NiCo$_2$S$_4$/NDCF electrode decrease gradually in the first 10 cycles, and then maintain at ~1250 mAh g^{-1} with no significant fading. After 100 cycles, the reversible capacity of NiCo$_2$S$_4$/NDCF electrode maintains as high as 1182 mAh g^{-1}, which is much higher than that of previously reported MSs electrodes.[16,17,57,58] In stark contrast, the NiCo$_2$S$_4$ powders pasted electrodes show continuous and progressive capacity fading along with the cycling under the same testing conditions, only retaining a discharge capacity of ~100 mAh g^{-1} after 50 cycles. Moreover, the Coulombic efficiency of NiCo$_2$S$_4$/NDCF electrodes increases sharply from 73.8% to nearly 100% as shown in Fig. 7(c), indicating that a stable SEI layer has already formed during the initial cycles.[18] Additionally, as shown in Fig. 7(d), the capacities of pure NDCF electrodes are much lower than those of NiCo$_2$S$_4$/NDCF electrodes even under lower current density of 200 mA g^{-1}, indicating that the NDCF substrates contribute little to the capacity of the composites.

The rate capability of the electrodes was further studied by cycling at different current densities ranging from 200 to 3200 mA g^{-1}, and finally returned back 200 mA g^{-1}. As shown in Fig. 7(e), the average discharge capacity of the NiCo$_2$S$_4$/NDCF electrode decreases from 1867 to 1518, 1251 and 1017 mAh g^{-1} when the current density is increased from 200 to 400 mA g^{-1}, 800 mA g^{-1} and 1600 mA g^{-1}, respectively. Notably, even at a high current density of 3200 mA g^{-1}, a favorable specific capacity of ~710 mAh g^{-1} can be maintained, illustrating the high rate capability of the NiCo$_2$S$_4$/NDCF composites. In comparison, the NiCo$_2$S$_4$ powders pasted electrode shows much lower capacities than the NiCo$_2$S$_4$/NDCF electrode, and exhibit obvious capacities fading when cycling at different current densities, indicating its worse rate capability. But the pure NDCF electrode exhibits stable capacities under cycling at different current densities, as shown in Fig. 7(e), manifesting its great significance on improving the rate capability of NiCo$_2$S$_4$. Moreover, after deep cycling at the high current density of 3200 mA g^{-1}, the specific capacities of NiCo$_2$S$_4$/NDCF electrode are nearly recovered to its initial values when the current density returned back to 200 mAg^{-1} after 50 cycles, manifesting their good reversibility. More importantly, when charged and discharged continuously at a current density of 200 mAh g^{-1} after the rate capability measurement, the NiCo$_2$S$_4$/NDCF electrodes maintain a stable high capacity of ~1500 mAh g^{-1}
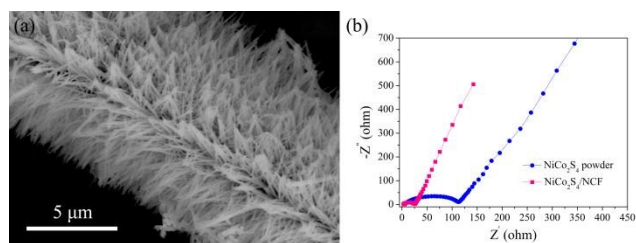
Fig. 8 (a) SEM images of the $NiCo_2S_4$/NDCF electrode after 100 cycles at a current density of 500 mA g^{-1}. (b) Nyquist plots of the $NiCo_2S_4$/NDCF and $NiCo_2S_4$ powders pasted electrodes in the frequency range of 100 kHz to 0.01 Hz

even after 150 cycles, further indicating their excellent cycling stability. In addition, the morphology of the $NiCo_2S_4$/NDCF electrode after 100 cycles at a current density of 500 mA g^{-1} is shown in Fig. 8(a). It can be seen clearly that the self-supported nanotube morphology retained well after the continuous cycling test, except some unavoidable aggregation of adjacent single nanotube, suggesting the good structural stability of the $NiCo_2S_4$/NDCF composites and the robust adhesion of the $NiCo_2S_4$ nanotubes on NDCF substrates.

To gain insight into the reason that $NiCo_2S_4$ nanotube arrays grown on NDCF possess such excellent lithium storage performance, electrochemical impedance spectroscopy (EIS) for the two electrodes was performed. Fig. 8(b) presents the Nyquist plots of $NiCo_2S_4$/NDCF and $NiCo_2S_4$ powders pasted electrodes, which are composed of a semicircle in the high-middle frequency region and a slope line in the low frequency region. The semicircle is attributed to the formation of the SEI layer and contacting impedance between active materials and electrolyte, and the charge-transfer resistance at the electrode/electrolyte interface.[52,59] And the slope line corresponds to Warburg diffusion into the bulk of the electrode, which is related to the diffusion-controlled process in the electrodes.[18,52,60] It is obvious that the size of the semicircle for the $NiCo_2S_4$/NDCF electrode is much smaller than that of the $NiCo_2S_4$ powders pasted electrode, suggesting that the $NiCo_2S_4$/NDCF electrode possesses the lower contacting impedance and electron-transfer resistances. Meanwhile, more vertical line in low-frequency region of the $NiCo_2S_4$/NDCF electrode compared to the $NiCo_2S_4$ powders pasted electrode indicates the faster Li^+ diffusion behavior of the $NiCo_2S_4$/NDCF composites, thereby resulting in the better electrode reaction kinetics during the charge/discharge process and superior cycling performance of the $NiCo_2S_4$/NDCF electrode as mentioned above. This results can be attributed to the integrated binder-free 3D electrode architectures, which avoids the use of any binder or conductive additives, offers a larger electrode/electrolyte contact area, and provides efficient 3D interconnected network pathways for both electron and ion.[10,19] Frankly, traditional binder-containing pasted electrodes have been demonstrated to present considerable resistance to electron transport and have a tendency to aggregate and form disconnected clusters during continuous charge-discharge

cycles, which further deteriorates electron conduction between the active materials and the current collector.[15] Meanwhile, it is less likely that an electrode consisting of binder and conductive carbon can provide a large and effective contact area between the active material and the electrolyte, maintain a short diffusion distance for Li^+ and accommodate mechanical strain during cycling.[18,60]

Based on the results above, the enhanced lithium-ion storage properties of the $NiCo_2S_4$/NDCF electrodes could be attributed to the unique material composition, the rationally designed nanostructure and the integrated smart architecture. Firstly, $NiCo_2S_4$ possesses inherently high electronic conductivity (~4 orders of magnitude higher than that of conventional MOs), higher electrochemical activity and capacity than mono-metal sulphides.[20-22] Meanwhile, benefiting from the nitrogen incorporation, the highly conductive NDCF substrate builds up an express pathway for fast electron transportation. And its porous 3D interconnected network architectures ensure $NiCo_2S_4$ in high contact with electrolyte, minimize transport distances between the composites and electrolyte, and further facilitate fast transportation of lithium ions and electrons, resulting in an excellent rate performance.[10,21,34] Besides, the well-designed hollow feature of the $NiCo_2S_4$ nanotubes is efficient to relief the volumetric expansion during the lithium insertion and extraction process, and the existence of voids in the nanotubes also provides sufficient free space to ameliorate the expansion tendency.[18] More importantly, compared with the traditional binder-containing pasted electrode, directly growing $NiCo_2S_4$ nanotubes on the skeleton of N-doped carbon foam with robust adhesion simplifies the electrode processing and improves utilization of the electroactive $NiCo_2S_4$ effectively. It is noteworthy that the integrated electrodes play a significant role in relieving the aggregation and mechanical failure of the $NiCo_2S_4$ during repeated charge-discharge process, ultimately reducing internal resistance, thereby enhancing the electrochemical performance of LIBs.[10] Benefiting from these advantages, the $NiCo_2S_4$/NDCF composites exhibit remarkable electrochemical performance, and hold great promise for high performance energy storage/conversion applications.

Conclusions

In summary, a novel $NiCo_2S_4$/NDCF composite has been successfully synthesized via a facile surfactant-assisted hydrothermal route and the subsequent sulfurization treatment, in which $NiCo_2S_4$ nanotube arrays are uniformly grown on the skeletons of NDCF substrates with robust adhesion. Such a well-designed composite judiciously combine the advantages of the $NiCo_2S_4$ nanotube arrays (high capacity, large specific surface area as well as effective relief of volumetric change) and 3D-structured NDCF substrate (high electronic conductivity, good flexibility, light weight, and fast mass and electron transport kinetics). When directly used as anodes for LIBs, the $NiCo_2S_4$/NDCF composites exhibit enhanced lithium storage properties compared to binder-containing counterparts,

This journal is © The Royal Society of Chemistry 2015

Phys. Chem. Chem. Phys., 2015, **00**, 1-3 **00**, 1-3 | **7**

with a high reversible capacity of 1721 mAh g^{-1} at a high current density of 500 mA g^{-1}, enhanced cycling performance maintaining a capacity of 1182 mAh g^{-1} after 100 cycles, and a remarkable rate capability.

Acknowledgements

Notes and references

1   B. Dunn, H. Kamath and J. M. Tarascon, *Science*, 2011, **334**, 928.

2   J. Liu, *Adv. Funct. Mater.*, 2013, **23**, 924.

3   N. S. Choi, Z. H. Chen, S. A. Freunberger, X. L. Ji, Y. K. Sun, K. Amine, G. Yushin, L. F. Nazar, J. Cho and P. G. Bruce, *Angew. Chem. Int. Ed.,* 2012, **51**, 9994.

4   M. J. Armstrong, C. O'Dwyer, W. J. Macklin and J. D. Holmes, *Nano Res.*, 2014, **7**, 1.

5   K. S. Kang, Y. S. Meng, J. Breger, C. P. Grey and G. Ceder, *Science*, 2006, **311**, 977.

6   A. Manthiram, *J. Phys. Chem. Lett.*, 2011, **2**, 176.

7   J. Jiang, Y. Y. Li, J. P. Liu, X. T. Huang, C. Z. Yuan and X. W. Lou, *Adv. Mater.*, 2012, **24**, 5166.

8   B. L. Ellis, P. Knauth, T. Djenizian, *Adv. Mater.*, 2014, **26**, 3368.

9   G. M. Zhou, F. Li and H. M. Cheng, *Energy Environ. Sci.*, 2014, **7**, 1307.

10 B. Wang, S. M. Li, X. Y. Wu, W. M. Tian, J. H. Liu and M. Yu, *J. Mater. Chem. A*, 2015, **3**, 13691.

11 W. Y. Li, L. N. Xu and J. Chen, *Adv. Funt. Mater.*, 2005, **15**, 851.

12 Y. G. Li, B. Tan and Y. Y. Wu, *Nano lett.*, 2008, **8**, 265.

13 H. Jiang, Y. J. Hu, S. J. Guo, C. Y. Yan, P. S. Lee and C. Z. Li, *ACS Nano*, 2014, **8**, 6038.

14 H. Jiang, D. Y. Ren, H. F. Wang, Y. J. Hu, S. J. Guo, H. Y.Yuan, P. J. Hu, L. Zhang and C. Z. Li, *Adv. Mater.*, 2015, **27**, 3687.

15 H. Y. Wang, D. Y. Ren, Z. J. Zhu, P. Saha, H. Jiang and C. Z. Li, *Chem. Eng. J.*, 2016, **288**, 179.

16 M. L. Mao, L. Jiang, L. C. Wu, M. Zhang and T. H. Wang, *J. Mater. Chem. A*, 2015, **3**, 13384.

17 Q. H. Wang, L. F. Jiao, Y. Han, H. M. Du, W. X. Peng, Q. N. Huan, D. W. Song, Y. C. Si, Y. J. Wang and H. T. Yuan, *J. Phys. Chem. C*, 2011, **115**, 8300.

18 R. J. Zou, Z. Y. Zhang, M. F. Yuen, M. L. Sun, J. Q. Hu, C. S. Lee and W. J. Zhang, *NPG Asia Materials*, 2015, **7**, e195.

19 L. W. Ji, Z. Lin, M. Alcoutlabi and X. G. Zhang, *Energy Environ. Sci.*, 2011, **4**, 2682.

20 J. W. Xiao, L. Wan, S. H. Yang, F. Xiao and S. Wang, *Nano Lett.*, 2014, **14**, 831.

21 H. C. Chen, J. J. Jiang, L. Zhang, D. D. Xia, Y. D. Zhao, D. Q. Guo, T. Qi and H. Z. Wan, *J. Power Sources*, 2014, **254**, 249.

22 L. F. Shen, J. Wang, G. Y. Xu, H. S. Li, H. Dou, and X. G. Zhang, *Adv. Energy Mater.*, 2015, **5**, 1400977.

23 H. Z. Wan, J. J. Jiang, J. W. Yu, K. Xu, L. Miao, L. Zhang, H. C. Chen and Y. J. Ruan, *CrystEngComm*, 2013, **15**, 7649.

24 J. W. Xiao, L. Wan, S. H. Yang, F. Xiao and S. Wang, *Nano Lett.*, 2014, **14**, 831.

25 Y. Liu, J. N. Zhang, S. P. Wang, K. X. Wang, Z. M. Chen and Q. Xu, *New J. Chem.*, 2014, **38**, 4045.

26 F. Zhu, H. Xia and T. Feng, *Adv. Funct. Mater.*, 2015, **30**, A53.

27 X. Yu, B. Lu, and Z. Xu, *Adv. Mater.,* 2014, **26,** 1044.

28 L. Taberna, S. Mitra, P. Poizot, P. Simon, J. M. Tarascon, *Nat.Mater.*, 2006, **5**, 567 .

29 C. G. Yang, D. W. Zhang, Y. B. Zhao, Y. H. Lu, L. Wang and J. B. Goodenough, *J. Power Sources*, 2011, **196**, 10673.

30 X. Cao, Z. Yin, and H. Zhang, *Energy Environ. Sci.*, 2014, **7**, 1850.

31 Z. Bo, W. G. Zhu, W. Ma, Z. H. Wen, X. R. Shuai, J. H. Chen, J. H. Yan, Z. H. Wang, K. F. Cen and X. L. Feng, *Adv. Mater.*, 2013, **25**, 5799.

32 J. Wang, J. Liu, D. Chao, J. Yan, J. Lin and Z. X. Shen, *Adv. Mater.*, 2014, **26**, 7162.

33 L. Zhao, L. Z. Fan, M. Q. Zhou, H. Guan, S. Y. Qiao, M. Antonietti and M. M. Titirici, *Adv. Mater.*, 2010, **22**, 5202.

34 X. S. Zhou, L. J. Wan and Y. G. Guo, *Adv. Mater.*, 2013, **25**, 2152.

35 H. P. Cong, S. Xin and S. H. Yu, *Nano Energy*, 2015, **13**, 482.

36 H. J. Fan, U. Gçsele and M. Zacharias, *Small*, 2007, **3**, 1660.

37 R. J. Zou, Z. Y. Zhang, M. F. Yuen, J. Q. Hu, C. S. Lee and W. J. Zhang, *Sci. Rep.*, 2015, **5**, 7862.

38 D. P. Cai, D. D. Wang, C. X. Wang, B. Liu, L. L. Wang, Y. Liu, Q. H. Li and T. H. Wang, *Electrochim. Acta*, 2015, **151**, 35.

39 H. C. Chen, J. J. Jiang, L. Zhang, D. D. Xia, Y. D. Zhao, D. Q. Guo, T. Qi and H. Z. Wan, *J. Power Sources*, 2014, **254**, 249.

40 M. Sun, J. J. Tie, G. Cheng, T. Lin, S. M. Peng, F. Z. Deng, F. Ye and L. Yu, *J. Mater. Chem. A*, 2015, **3**, 1730.

41 Y. S. Lin and J. G. Duh, *J. Power Sources*, 2011, **196**, 10698.

42 X. Y. Wu, S. M. Li, B. Wang, J. H. Liu and M. Yu, RSC Adv. 2015, **5**, 81341.

43 Q. H. Wang, L. F. Jiao, H. M. Du, Y. C. Si, Y. J. Wang and H. T. Yuan, *J. Mater. Chem.*, 2012, **22**, 21387.

44 Y. F. Zhang, C. C. Sun, H. Q. Su, W. Huang and X. C. Dong, *Nanoscale*, 2015, **7**, 3155.

45 S. Zhuo, Y. Xu, W. Zhao, J. Zhang and B. Zhang, *Angew. Chem. Int. Ed.*, 2013, **52**, 8602.

46 J. Park, H. Zheng, Y. Jun and A.P. Alivisatos, *J. Am. Chem. Soc.*, 2009, **131**, 13943.

47 H. C. Chen, J. J. Jiang, L. Zhang, H. Z. Wan, T. Qi and D. D. Xia, *Nanoscale*, 2013, **5**, 8879.

48 H. Z. Wan, J. J. Jiang, J. W. Yu, K. Xu, L. Miao, L. Zhang, H. C. Chen and Y. J. Ruan, *CrystEngComm*, 2013, **15**, 7649.

49 Y. C. Du, X. S. Zhu, X. S. Zhou, L. Y. Hu, Z. H. Dai and J. C. Bao, *J. Mater. Chem. A*, 2015, **3**, 6787.

50 S. F. Kong, Z. T. Jin, H. Liu and Y. Wang, *J. Phys. Chem. C*, 2014, **118**, 25355.

51 R. H. Wang, C. H. Xu, J. Sun, Y. Q. Liu, L. Gao, H. L. Yao and C. H. Lin, *Nano Energy*, 2014, **8**, 183.

52 N. Mahmood, C. Z. Zhang, J. Jiang, F. Liu and Y. L. Hou, *Chem. Eur. J.*, 2013, **19**, 5183.

53 L. Zhou, D. Y. Zhao, and X. W. Lou, *Adv. Mater.*, 2012, **24**, 745.

54 J. Bai , X. G. Li , G. Z. Liu , Y. T. Qian , and S. L. Xiong, *Adv. Funct. Mater.*, 2014, **24**, 3012.

55 B. S. Li, J. K. Feng, Y. T. Qian and S. L. Xiong, *J. Mater. Chem. A*,

8 | *Phys. Chem. Chem. Phys.,* 2015, **00**, 1-3

This journal is © The Royal Society of Chemistry 2015

2015, **3**, 10336.

56 R. C. Jin, D. M. Liu, C. P. Liu and G. Liu, *RSC Adv.*, 2015, **5**, 84711.

57 K. Chang and W. X. Chen, *ACS Nano*, 2011, **5**, 4720.

58 D. Zhang, Y.J. Mai, J.Y. Xiang, X.H. Xia, Y.Q. Qiao and J.P. Tu, *J. Power Sources*, 2012, **217**, 229.

59 D. Aurbach, *J. Power Sources*, 2000, **89**, 206.

60 H. Liu, Z. Bi, X. G. Sun, R. R. Unocic, M. P. Paranthaman, S. Dai and G. M. Brown, *Adv. Mater.*, 2011, **23**, 3450.

This journal is © The Royal Society of Chemistry 2015

Phys. Chem. Chem. Phys., 2015, **00**, 1-3 **00**, 1-3 | **9**